# Unsteady Flow Evolution Through a Turning Midturbine Frame Part 1: Time-Resolved Flow

D. Lengani,* R. Spataro,† B. Paradiso,‡ and E. Göttlich§
*Graz University of Technology, A-8010 Graz, Austria*

## Nomenclature

| | | |
|---|---|---|
| $C$ | = | blade axial chord |
| $C_p$ | = | static pressure coefficient |
| $Cp_T$ | = | total pressure coefficient |
| $H$ | = | relative channel height |
| $h$ | = | channel height |
| $m_{r,\text{in}}$ | = | reduced mass flow, stage inlet |
| $n_{r,\text{in}}$ | = | reduced rotational speed, stage inlet |
| $p$ | = | static pressure |
| $p_{\text{din}}$ | = | dynamic pressure |
| $p_T$ | = | total pressure |
| $R$ | = | radius |
| $Re$ | = | Reynolds number |
| $T$ | = | blade passing period |
| $t$ | = | time |
| $v$ | = | velocity |
| $\theta$ | = | circumferential coordinate |
| $\rho$ | = | flow density |
| $\omega_{\text{sv}}$ | = | streamwise vorticity |
| <> | = | deterministic periodic component |

*Subscript*

| | | |
|---|---|---|
| av | = | averaged properties |

*Superscripts*

| | | |
|---|---|---|
| – | = | time-averaged properties |
| ~ | = | phase-locked properties |
| ′ | = | stochastic fluctuating component |

## I. Introduction

THE performance of turbomachinery strongly depends on the periodic unsteady interactions between stator and rotor rows. Even though it is well known that the accuracy of computational models depends on their ability to account for deterministic and stochastic unsteadiness (e.g., Adamczyk [1], He [2], and Tucker [3]), the aerodynamic design is often still made only considering steady flows in their own frame of reference, which are averaged in the transformation across reference frames (e.g., the "mixing plane" of the model of Denton and Singh [4] or the axisymmetric term in the model of Adamczyk [5]). This is becoming a major limitation from the point of view of multi-objective optimization. The aerodynamic efficiency of current turbines is so high that taking into account unsteady flow issues seems to be the route for possible performance increases (Hodson et al. [6]). Similarly, some components such as the high-pressure stage(s) cause large unsteady pressure amplitudes [7] and possible stress and noise problems because they are highly loaded and transonic.

A component that has a critical impact on the overall performance of modern and future generation aeroengines is the diffusing duct, which connects the high-pressure (HP) to the low-pressure (LP) turbine frame. A midturbine frame consisting of a diffusing duct with bulky structural turning vanes (struts) could be used as a part of the engine mount as well as a swirler for the downstream turbine. This would lead to shorter and lighter engines. Furthermore, a new concept of integrated design, which combines the mechanical function of a strut with the aerodynamic performance of an LP vane, has recently been demonstrated (e.g., [8,9]). In this configuration, the first LP stage is composed of the intermediate turbine diffuser populated with turning vanes and an LP rotor at the outlet of the duct.

The fundamental aerodynamics of such component has been intensively studied in the last 15 years. There are too many investigations to be exhaustively mentioned here, however, the interested reader may find a complete literature review in the paper of Göttlich [10]. It

Received 12 June 2014; revision received 6 February 2015; accepted for publication 12 May 2015; published online 1 October 2015.

*Institute for Thermal Turbomachinery and Machine Dynamics; currently Dipartimento di Ingegneria Meccanica, Energetica, Gestionale e dei Trasporti, Università di Genova 16146 Genova, Italy; davide.lengani@edu.unige.it.

†Institute for Thermal Turbomachinery and Machine Dynamics; currently Whittle Laboratory, Department of Engineering, University of Cambridge, Cambridge, England CB2 1TN, United Kingdom; rs801@cam.ac.uk.

‡Institute for Thermal Turbomachinery and Machine Dynamics; currently Dipartimento di Energia, Politecnico di Milano 20133 Milano, Italy.

§Institute for Thermal Turbomachinery and Machine Dynamics; emil.goettlich@tugraz.at (Corresponding Author).

has been shown that the aerodynamic performance of the turbine diffuser depends on parameters such as the diffusion rate, the presence of vanes within the duct, the magnitude of the inlet swirl, the shape of the meridional flowpath, and the inlet boundary-layer profile. The current state of the art should allow the design of a diffusing duct that leads the flow to the first LP rotor without separation or large nonuniformity. The aerodynamics of such a component can be simplified and studied in terms of the time-mean flow properties. However, a multidisciplinary optimization of it can be obtained only by looking into details of the unsteady interactions. The inlet flow to the duct is, in fact, dominated by the flow structures evoked by the HP stage. As previously mentioned, at the outlet of this stage, there are large unsteady pressure fluctuations that are caused by the shock waves and the secondary flows (e.g., Dénos and Paniagua [11]). This is because a typical HP turbine has a very low aspect ratio and its outflow is typically supersonic in the relative frame of reference.

There is a limited number of openly published works that analyze the impact of these unsteady effects on a downstream component in a realistic configuration (e.g., Miller et al. [12,13], Davis et al. [14], Haldeman et al. [15], Göttlich et al. [16], and Lavagnoli et al. [17]). As observed in Miller et al. [13] and in Göttlich et al. [16], the first bend of the duct induces a radial pressure gradient on the flow, which makes the high-entropy fluid from the HP stage migrate to above 50% of the passage height. Hence, the largest unsteady effects are commonly observed in this portion of the duct channel. Particularly, in the case of unshrouded HP turbines, the rotor tip leakage flow causes the strongest interactions with the following vane, which may lead to the suppression of its upper passage vortex as observed in Miller et al. [12]. Furthermore, the complex system of secondary vortices, together with the blade leading-edge shocks, determines the extent of the unsteady pressure fluctuations on the duct vane. Also, the relative position of the HP vane and duct vane, known as clocking, plays a major role in the unsteady interactions [15]. The clocking effect was found to influence the location of maximum unsteady fluctuations on the vane/strut surfaces, but it is difficult to select a position of clocking that minimizes the overall unsteadiness.

Recently, an engine-relevant test setup for turning midturbine frames (TMTFs) with up- and downstream turbine stages with counter-rotating rotors has been developed at Graz University of Technology. Previously published results from this facility in different configurations (baseline TMTF in Lengani et al. [18,19] and TMTF with splitter vanes in Spataro et al. [20,21]) have focused their attention on the unsteadiness at the outlet of the LP stage. They have shown that angle and velocity fluctuations of the HP stage decay quickly in the front part of the diffusing duct. In contrast, the unsteady pressure perturbation from the HP rotor periodicity contributes considerably to the overall pressure fluctuations at the exit of the duct.

The present paper, which is divided in two parts, extends the analysis of the baseline TMTF configuration proposed by Lengani et al. [19]. The purpose of this two part paper is a detailed discussion of the unsteady flow propagation within the duct. This is carried out considering experimental data together with validated computational fluid dynamics (CFD) results and following their temporal and spatial evolution from the outlet of the HP rotor to the inlet of the LP rotor. To this end, complementary measurement techniques are used in this first part paper [i.e., fast-response aerodynamic pressure probe (FRAPP) and fast-response pressure sensors (Kulite) mounted below the strut surface and connected to it via a small hole (0.8 mm)]. Full area traverses with the FRAPP are performed up- and downstream of the duct and full vane–vane clocking effects are measured with Kulite sensors. The main focus of the first part paper is to identify the relative effects of secondary flows, shock waves, and clocking on the unsteady fluctuations of the TMTF by means of CFD together with these experimental results. In this paper, the complex interactions are discussed considering the unsteadiness related to the HP rotor only. The second part of the paper [22] will extend this analysis by means of one- and two-dimensional (2-D) Fourier analysis, which will account for any source of deterministic stresses measured within this facility.

This first part of the paper is structured as follows:

1) Methodology, facility, CFD, and measurement techniques are reported.

2) The first section of the results compares CFD and FRAPP data in the measurement plane upstream of the TMTF, introducing some known literature results as the inlet boundary conditions to the duct.

3) In the second part of the result section, the propagation of the unsteady flow features within the duct and along the strut surfaces is discussed on the basis of CFD and experimental results.

## II. Experimental Apparatus and Methodology

### A. Facility Description

The transonic test turbine facility is a continuously operating two-stage cold-flow, open-circuit plant, which consists of a transonic HP stage and a counter-rotating LP stage (a schematic drawing is shown in Fig. 1). This unique configuration allows the testing of rig inserts under engine representative conditions. The power output of the HP stage is used to drive a three-stage radial brake compressor, whereas the power of the LP turbine is absorbed by a water brake with a maximum power of 700 kW. Both turbines are designed with overhung-type turbine shafts and the LP turbine is mounted on an axially movable frame. This allows easy disk assembly without dismantling the bearings and the simple application of transition ducts and TMTF designs with different axial lengths. The facility is driven by pressurized air delivered by a separate 3 MW compressor located in the second basement of the building. Further details on the facility and on the configuration of the two stages may be found in Hubinka et al. [23,24]

### B. Test Setup and Operating Conditions

Table 1 displays the main design parameters for the HP and LP stages (TMTF + LP rotor); the design of it was provided by MTU Aero Engines. The HP turbine consists of 24 vanes and 36 blades. For the LP stage, a blade count of 16 struts and 72 blades was chosen.

The HP vanes as well as the outer casing downstream of the TMTF struts are fully rotatable in the circumferential direction. This enables area traverses for probe and rake measurements in the four planes identified in Fig. 1. Table 1 lists the main parameters of the operating point. The investigated aerodesign has an overall pressure ratio of four. The total pressure ratio is three for the HP turbine and 1.3 for the LP turbine. The HP vanes are operating under choked conditions. The absolute Mach number at the TMTF inlet of about 0.5 is representative of realistic duct inlet conditions of modern jet engines with a single-stage HP turbine at the cruise operating point. These are the same operating conditions and test setup of previous publications (Lengani et al. [18,19]).

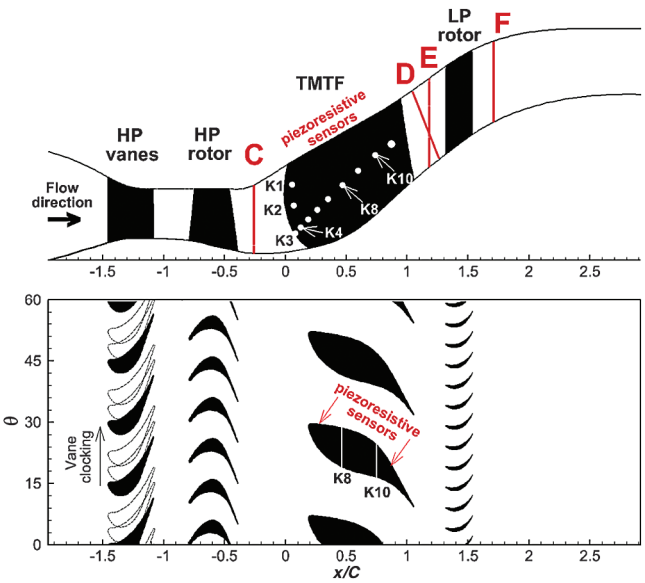


**Fig. 1 Two-stage turbine test rig with measurement locations.**

**Table 1 Blading parameters and operating conditions**

| Test setup | | | | |
|---|---|---|---|---|
| *Blading parameters* | | | | |
| | HP vane | HP blade | TMTF | LP blade |
| Vane/ blade no. | 24 | 36 | 16 | 72 |
| $h/C$ | 1.15 | 1.37 | 0.53 | 2.94 |
| $Re(10^{-6})$ | 2.38 | 1.1 | 1.86 | 0.46 |
| Tip gap | — — | Unshrouded | — — | Shrouded |
| *Operating conditions* | | | | |
| | HP stage | | LP stage | |
| $n_{r,\text{in}}$, rpm/$\sqrt{K}$ | 524.4 | | 195.3 | |
| $m_{r,\text{in}}$, kg/s · $\sqrt{K}$/(bar) | 81.2 | | 214.6 | |
| Stage $p_T$ ratio | 3 | | 1.3 | |
| Power, kW | 1710 | | 340 | |

### C. Measurement Techniques

Unsteady flow measurements were performed by means of different fast-response aerodynamic pressure probes (see Spataro et al. [21]). The present paper describes the results obtained with a cylindrical one-sensor probe (see Persico et al. [25] for more details). The aerodynamic accuracy of the probe was evaluated in a calibrated nozzle, resulting in an extended uncertainty equal to ±0.5% of the kinetic head for the pressure measurements, ±0.3 deg for the flow angle, and ±0.3% of the measured value for the Mach number. Details on the transfer function of the probe are given in [25], where the probe was calibrated in a low-pressure shock tube. The probe bandwidth is up to 80 kHz, after digital compensation.

The present paper describes the results obtained by the fast-response probe in annular sectors in planes C and D (marked in Fig. 1). Plane C is a plane perpendicular to the horizontal direction and is located at 77% of the HP rotor chord downstream of the HP blade trailing edge, whereas plane D (discussed only in part 2 [22]) is inclined by 110 deg to the horizontal direction and, at midspan, its distance from the vane trailing edge (TE) is 14% of the strut axial chord. For plane D, the full area traverses were performed over one strut pitch (22.5 deg), with a measurement grid of 19 positions along the blade span and of 46 positions over one pitch of the strut ($\Delta\theta_{\text{strut}}$). Unlike in planes D or F, where the probe was traversed circumferentially, in plane C, the pitchwise effect due to the upstream vanes were measured keeping the probe at a fixed angular position and rotating the HP vane ring to cover one stator pitch. The measurement grid in plane C counts for 21 points radially and 21 points circumferentially.

The unsteady flowfield through the TMTF was investigated by means of 11 piezoresistive sensors, Kulite XCE-0.62 (sensors K1–K10) and Kulite LE-062-25A (sensor K11) (linear frequency range $\Delta f = 0 - 20$ kHz), aligned along a streamline visible in Fig. 1. Sensors K1–K3 were placed at the strut leading edge to measure the unsteady spanwise variation of the flow pressure fluctuations, whereas sensors K3–K11 were placed parallel to a streamline where the CFD prediction showed a possible transition occurrence. The sensor position coordinates are presented in Table 2. The measurements with the Kulite sensors were performed for 30 different circumferential positions of the HP vane (which is movable). The circumferential traversing of the HP vane covers 15 deg (with a step of 0.5 deg), which corresponds to the complete analysis of the clocking of HP vane and struts. The accuracy of the pressure sensors was evaluated in a calibration environment, resulting in an extended uncertainty that does not exceed ±5% of the local pressure fluctuations. The largest errors were observed for sensors K5 and K9 for some clocking positions, otherwise, the typical relative uncertainty is ±2% of the measured unsteady pressure.

**Table 2 Position of fast-response pressure sensors**

| Sensor position on the strut suction surface | | | | | |
|---|---|---|---|---|---|
| Sensor | Span, $H$ | $x/C$ | Sensor | $H$ | $x/C$ |
| K1 | 0.70 | 0.05 | K7 | 0.43 | 0.35 |
| K2 | 0.50 | 0.07 | K8 | 0.50 | 0.47 |
| K3 | 0.19 | 0.08 | K9 | 0.55 | 0.60 |
| K4 | 0.24 | 0.12 | K10 | 0.59 | 0.74 |
| K5 | 0.30 | 0.18 | K11 | 0.63 | 0.84 |
| K6 | 0.37 | 0.26 | — — | — — | — — |

### D. Data Reduction

Data, for both Kulite and FRAPP, are acquired at 200 kHz for 2 s, which corresponds to more than 100 revolutions of the LP turbine and more than 350 of the HP turbine. Phase averaging, in the present paper, was performed by triggering the flow with the shaft encoder of the HP rotor according to the triple decomposition procedure [26], for a generic variable $p$:

$$p(t) = \bar{p} + < p > + p'(t) \tag{1}$$

where $< p >$ is the purely periodic component associated with a coherent periodic structure and $p'(t)$ is the random fluctuation associated mainly with turbulence. This decomposition is used to characterize the periodic unsteadiness induced by the HP rotor. In the case of the Kulite, the phase-resolved fluctuations of pressure are the direct results of this procedure. For the FRAPP, the determination of the flow properties is made possible after phase averaging: the periodic fluctuations of velocity, pressures, and flow angles are determined at each phase from the phase-averaged values of the three rotations of the probe.

This first part paper is focused on the analysis of the unsteadiness induced by the HP rotor; the HP shaft encoder only is used for the triple decomposition. The second part of the paper [22] will extend this analysis, reconstructing a phase that takes into account the relative rotor–rotor positions (as introduced in Lengani et al. [19]). The FRAPP signal and the two shaft encoders were acquired simultaneously for this further analysis, which will be discussed in detail in the companion paper [22].

### E. Numerical Techniques

The numerical investigation was performed by a commercial CFD code (CFX 12.1). The computational grid consists of 16.7 million elements divided in five domains (two rotating for the rotors and three stationary for the vanes and the outflow), all of them with 90 deg periodicity. The mesh adopted for the unsteady computation is similar to the mesh provided in Spataro et al. [27] for a steady computation but extended to the 90 deg periodicity and to the HP stage.

The unsteady simulation required about 28 GB of memory. The code solves the Navier–Stokes equation system with first-order accuracy in areas where the gradients change sharply to prevent overshoots and undershoots and maintain robustness, and second order in flow regions with low variable gradients to enhance accuracy [28]. The turbulence model used was the shear stress transport $k$-$\omega$ model by Menter [29]. The unsteady flow was computed by second-order backward equations; it is a robust, implicit, conservative in time, computational scheme [28]. The time step was chosen as 1/100th of the high-pressure rotor blade passing period. The conditions at the inlet and outlet boundaries were taken from the experimental measurements performed by Santner et al. [30] and Hubinka et al. [24].

## III. Results

This section is organized in two main parts. First, the flow structures in plane C (at the inlet of the duct) are introduced. The results of this plane confirm some of the well-known findings about the main flow patterns observable downstream of HP stages. This analysis is intended to identify such features in this setup to help the understanding of the measured and predicted data. The second section is introduced by a small summary of the time-mean flowfield developing within the duct, identifying the main sources of the pressure gradients (such features were described in detail in Spataro et al. [27]). The results provide a description of the unsteady flow propagation starting from a panoramic view of the Kulite measurements in comparison with CFD. This section ends with a discussion aimed

at simplifying the description of the principal source of unsteady effects: secondary flows, shock waves, clocking, and local effects of velocity and pressure gradient on the amplification of the induced unsteady fluctuations.

### A. Plane C, HP Rotor Outlet

#### 1. *Time-Mean Flow*

The upstream HP turbine is a low-aspect-ratio stage with an unshrouded rotor. The outlet time-mean flow was described in previous publications [27,31] based on experimental results obtained with a five hole probe. This section provides a brief summary of the time-mean CFD results before introducing the time-resolved flow.

Figure 2 shows the time-averaged CFD results of the non-dimensional total and static pressure ($Cp_T$ on top and $Cp$ on bottom, respectively). The contour plots of these quantities are shown on the left side, whereas on the right side, their mass-average distribution is depicted. The spanwise location is plotted in terms of normalized channel height $H$. The total pressure is shown in terms of $Cp_T$ which was defined as follows:

$$Cp_T = \frac{p_T - \bar{p}_{T,C}}{\bar{p}_{T,C} - \bar{p}_C} \tag{2}$$

where the subscript $C$ indicates the area averaged values in plane $C$.

A similar definition is applied for the static pressure coefficient $Cp$, with the exception that the numerator is defined by substituting the term $p_T$ with the static pressure $p$.

The flowfield is characterized by total and static pressure gradients in both the radial and circumferential directions. In the time-averaged flowfield, the horizontal stripes are the time-mean effect of the rotor structures, whereas the circumferential nonuniformities may be attributed to the stator flow structures and their interaction with the rotor. Furthermore, the presence of the rotor tip leakage vortex (TLV) and the rotor low-passage vortex (LPV) can be detected, where sharp changes in the spanwise distributions of the total pressure are observed. Starting from these considerations, it is reasonable to assume the locations of the TLV at $H \cong 0.9$, where there is a uniform blue stripe in the contour plot of $Cp_T$ (top of Fig. 2) and a sharp gradient in its mass-averaged spanwise distribution. Similarly, the LPV can be identified at around $H \cong 0.48$. In the lower half of the channel, the map of total pressure shows the effects of the HP vanes' interaction of stator secondary flows, wakes, and shocks with the rotor.

The static pressure contour plot ($C_p$ on bottom of Fig. 2) shows that the circumferential pressure gradient has a low amplitude and its azimuthal periodicity is related to the interaction of the two vane rows. Otherwise, the radial pressure gradient is the most evident feature in the $Cp$ distribution plot. In a conventional axial turbine, the radial equilibrium gradient due to the imposed swirl pushes the flowfield toward the hub. Here, the presence of the first duct bend plays a major role: the flow is pushed toward the casing where higher flow velocities, higher Mach number, and higher total pressure levels can be observed.

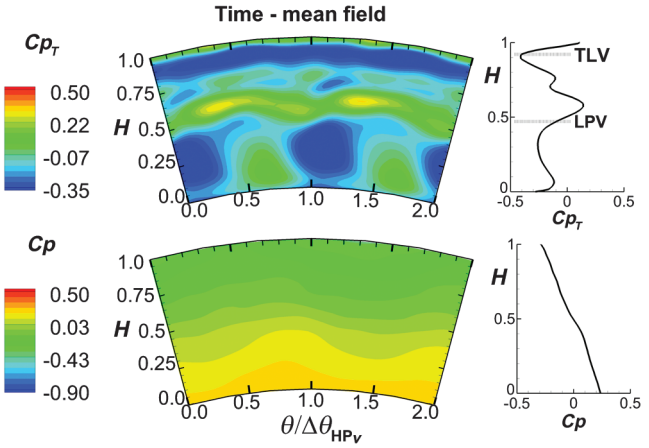


**Fig. 2 Plane C: numerical time-mean flowfield at the TMTF inlet.**

#### 2. *Unsteady Flow Features*

The flow structures that characterize the duct inlet are better described considering the time-resolved flow. In fact, secondary flows, wakes, and shock waves of the HP rotor move together in the circumferential direction and they are modulated in strength by the interaction with the upstream vane. The results in this section are aimed at the identification of the principal structures, which leaves the rotor and the validation of the CFD results with the FRAPP data. A more extensive description of an HP rotor outlet flow in a realistic configuration with a downstream diffusing duct may be found in the aforementioned publications (e.g., [13,16]).

The validation of the CFD with the experimental data is provided at a selected circumferential position (a more exhaustive validation will be provided in part 2 [22]). Figure 3 shows a time-space plot of the time-resolved total pressure coefficient, which is computed as described in Eq. (2) from the time-resolved (CFD) and phase-averaged (FRAPP) total pressure. In these plots, the normalized spanwise position $H$ is plotted on the ordinate, whereas the normalized timescale $t/T$ is plotted on the abscissa, with $T$ referring to the HP blade passing period. Two consecutive blade passing periods are represented to improve the readability of the pictures. These results are presented for corresponding circumferential positions and the relative phase of CFD is adjusted to match that of the FRAPP data.

The largest deficit of total pressure is observed, as expected, around the tip leakage vortex position (marked on the pictures as TLV). The two results match quite well in terms of magnitude and position. Note that the tip gap size implemented in the CFD model is obtained by means of a correlation between the measured cold gap and the gap in operation developed from tests in a previous setup of the facility (see Göttlich et al. [16], where the influence of blade tip gap variation is also described).

The agreement with experimental data is quite good for the portion of the plane above midspan. The largest discrepancies are observed on the bottom half of the channel. The $Cp_T$ trace of the lower passage vortex (marked as LPV) matches quite well in terms of position but less well in magnitude. Below the position of the LPV, the total pressure fluctuations are mainly due to the rotor wakes and shock waves that induce successive (in time) low and high values of the $Cp_T$. In this circumferential position, the experimental data seem to identify a larger number of these events in time than the CFD. The CFD is not correctly modeling the shock reflections and interactions that occur at the highest frequencies. This is a common

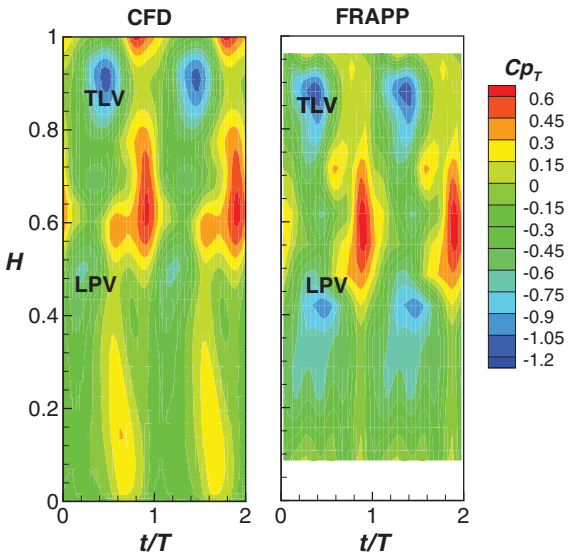


**Fig. 3 Time-space plots of time-resolved total pressure coefficient; comparison between CFD and FRAPP data for a fixed circumferential position.**

shortcoming of many computational tools, which tend to smear gradients, underpredicting the amplitude of the higher order harmonics. It is also unsurprising that the tip flow is better modeled than the root flow. The tip vortices form at a known sharp edge, whereas the root vortices are a product of unstable saddle flows (separations) at the wall, which are very sensitive to the details of the boundary-layer state.

The $Cp_T$ distribution is used as validation because the total pressure is a quantity that is directly measured experimentally and accounts for the effects of all flow features. However, the identification of the exact position of the flow structures can be better performed by taking into account for different variables. To identify the secondary vortices and shock system, time snapshots of streamwise vorticity and of static pressure are plotted in Fig. 4.

The streamwise vorticity (Fig. 4a) is suitable for the identification of the vortical structures within the flow. Similarly, the wake of the blades can be identified and they are marked on the picture with white dotted lines (for both plots of Fig. 4).

As discussed in the previous section, the radial pressure gradient pushes the flow structures upward. The nuclei at high and low vorticity are located above 40% span. This series of nuclei identifies several vortices. The secondary flow system is characterized by the passage vortices, the tip leakage vortex, and leading-edge streamwise shed vortices [16]. The main vorticities representing the LPV and TLV can be seen corotating. The structures also show a small circumferential modulation due to the interaction of the rotor with the upstream stator.

The shock system is identified by the time-resolved static pressure field at the transition duct inlet (Fig. 4b). The time snapshot shown in the figure confirms the effect of the downstream bend on the radial pressure distribution, whereas the main fluctuations in the circumferential direction are related with the rotor blade passing period. The dotted white lines help identify the blade wakes around which sharp pressure gradients of the static pressure are observed. Large circumferential pressure gradients characterize the whole channel height, and the direct shock wave front or smaller reflected shocks can be identified according to the relative position of the HP blade and stator rows. More details on such unsteady flow features downstream of a similar HP turbine may be found in Paradiso et al. [32]. The present test case differs from the one of Paradiso et al. [32] because of the downstream diffusing duct and strut. Even though the modulation of the outlet shock system is mainly due to the interaction with the upstream vane, there is an effect on the shock distribution attributable to the downstream components.

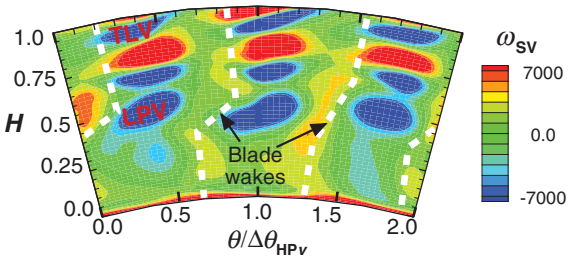


a) Snapshot of time-resolved vorticity

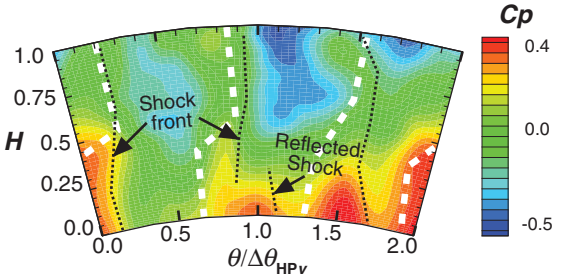


b) Snapshot of time-resolved pressure coefficient

**Fig. 4 Unsteady CFD: time-resolved flowfield in plane C (view from downstream; blade rotation direction is clockwise).**

## B. TMTF Flow

### 1. *Summary of the Time-Mean Flow*

Before discussing the unsteady flow features, a brief summary of the time-mean flow through the TMTF is reported here. A detailed discussion of it may be found in Spataro et al. [27]. For completeness, the distribution of the time-mean static pressure coefficient $Cp$ is depicted in Fig. 5 for a blade-to-blade plane at 50% span. The largest values of this coefficient are measured at the stagnation point at the strut leading edge (LE). The potential pressure field can be identified by the region at high static pressure that extends upstream. The minimum of $Cp$, which corresponds to the maximum velocity, is observed at the suction side (SS) for the position of sensor K10 as marked on the plot.

Further sources of the pressure gradients acting on the fluid are as follows [27]:

1) The first bend of the meridional path (upstream of the LP vane) generates a pressure distribution that pushes the flow toward the casing. The same effect is already observed on the flow structures evoked by the HP stage, as discussed in the previous section.

2) The deflection imposed to a flow in an annular configuration generates a suction-to-pressure side (PS) gradient and a radial pressure gradient. The latter pushes the fluid toward the hub endwall and its impact will increase with the increasing turning induced by the strut (swirl effect).

3) The second bend of the meridional flowpath located downstream of the TMTF path pushes the flow toward the hub.

4) The three-dimensional (3-D) design of the vane (lean and sweep distribution) also influences the spanwise pressure gradients, as extensively studied in literature.

The results of Spataro et al. [27] showed that the main vortical structures coming from the upstream stage are convected and transported to the inlet of the downstream turbine instead of decaying as would be expected in a corotating–rotors setup. Moreover, whereas the upper part of the TMTF channel shows a confined vane upper passage vortex, no "traditional" passage vortex is created in the lower part of the channel. Indeed, the swirl induced by the turning struts leads to a large vortex that, taking into consideration the aft-loaded design of the vane, develops later on in the passage and extends over the full channel height.

### 2. *Experimental Results*

Figure 6 shows the comparison between the unsteady CFD and the pressure sensors phase-averaged results. The comparison is presented for one clocking position (reference position, clock. "24") by means of the Kulite sensors installed along a well-defined line (sensors 4, 6, 8–10). For completeness, the experimental results are shown for a second clocking position, corresponding to the adjacent strut suction side (clock. "9"). The clocking was performed by altering the HP vane position. The rotor trigger has not been adjusted during the postprocessing phase. As a consequence, the measurement

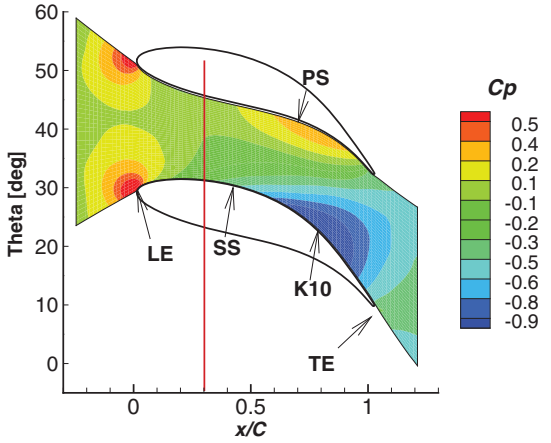


**Fig. 5 Time-mean static pressure coefficient; CFD results in the blade-to-blade plane at 50% span, TMTF.**

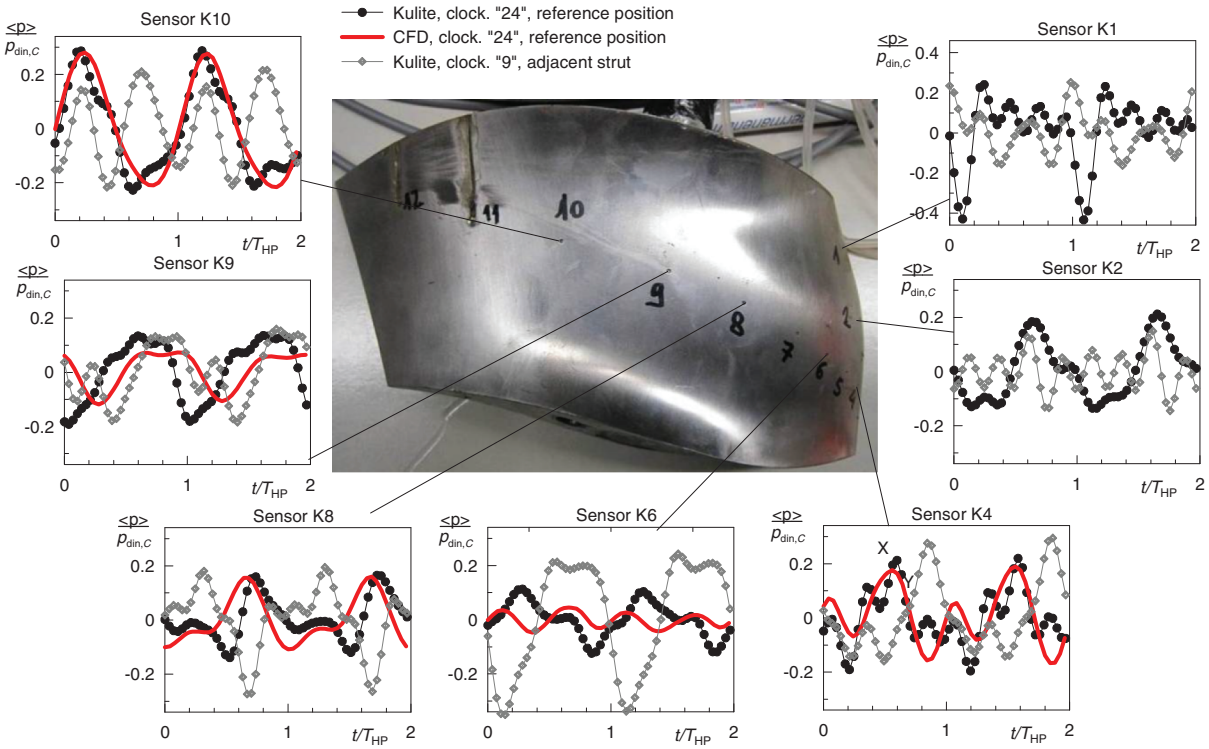


**Fig. 6 Unsteady pressure fluctuations through the strut; comparison between CFD and Kulite data.**

starts at a different stator–rotor position and the structures do not appear at the same time for the two different clocking positions.

The normalized timescale $t/T$ is plotted on the abscissa of the plots; two consecutive blade passing periods are represented to improve the readability of the pictures. The purely deterministic fluctuations of pressure [$< p >$, see Eq. (1)], which is made nondimensional by the average dynamic pressure of plane C, is shown in the ordinate. The figure should be read from right to left, following the flow direction from the leading edge to the trailing edge of the strut.

The first three sensors (K1, K2, and K4) show the fluctuations induced in the strut leading edge at the tip, midspan, and hub, respectively. Comparing the three sensors, the largest amplitude of the pressure deterministic fluctuation is measured for sensor K1 at the tip (note that the scale of the ordinate is different than the other subplots). The sensors K1 of the reference position (clocking position 24) shows a large deficit of pressure due to the passing of the rotor tip leakage vortex and rotor wake. It is interesting to observe a large deviation from this result for the adjacent strut suction side (clock. position 9), where this large deficit of pressure is not observed. Indeed, the effect of indexing the HP vane and LP strut alters the convection of all the flow structures. The amplitude of the pressure fluctuations decreases for sensors K2 and K4. In these cases, the effect of clocking does not alter the amplitude of the maximum pressure fluctuation but mostly its time-resolved evolution. For K2, the time signal of the reference position has just 1 maximum per blade passing period, whereas the adjacent strut presents 4 maxima. The opposite situation can be observed in sensor K4. Below 50% span, as previously discussed, the rotor outlet flow is dominated by the shock wave system. The modulation of the HP vane makes the phase lag between reflected and direct shocks vary. Moreover, pressure fluctuations may be locally produced by the von Kármán vortices of the blade wake, because they are phase locked to the rotor passing [33], or shed vortices or interactions with the secondary flows of the upstream vane (see for example Miller et al. [13] for more details). The Kulite results at the strut leading edge show how this complex patterns impingement strongly depends on the vane–vane position and changes with the strut span, hence 3-D effects play a major role in this interaction.

Sensor K4 shows also the first comparison between CFD and experimental data. The agreement, in terms of amplitude, is very good; however, the number of structures (the maxima in the pressure distribution) impinging on the strut surface is slightly underpredicted by the CFD. The agreement with the experimental data improves moving downstream. The following sensors (from K6 to K10) show very similar amplitudes of the pressure fluctuations where the maximum deviation of CFD results from experimental data occur at K6 and K9. Otherwise, the difference between the two results, in terms of maximum amplitude, stays within 20% of the experimental value of the static pressure fluctuation. The agreement between CFD and Kulite is also good in terms of relative phase. It should be noted that all the CFD results have been shifted by a portion of a blade passing period to make them fit with the experimental one in position K4. As a consequence, the fact that the relative phase between the CFD and Kulite signal has a good fit for the following measurement positions means that the computation predicts reasonably well the propagation of the flow structures, if not their initial arrival at the strut.

The experimental results for the two clocking positions of the last sensors (from K6 to K10) highlight the strong dependency of the pressure field within the strut passage on the vane–vane relative position. In fact, for the reference clocking position, the amplitude of the pressure fluctuations is increasing from position K6 to K10. The trend is the opposite for the adjacent suction side (clocking 9). Moreover, the energy content at high frequency, such as the 4 maxima of K1 and K2 (which correspond to the fourth harmonic of the blade passing period), tends to decay downstream. In position K10, the clocking 9 still presents high amplitudes at the doubled blade passing frequency (2 maxima within one blade passing period).

### 3. *CFD Results*

Blade-to-blade planes at different span heights and a meridional plane are extracted to understand the different effects that characterize the propagation of the deterministic unsteady fluctuations within the strut passage. Figure 7 shows results from blade-to-blade surfaces at 50 and 30% span (Figs. 7a and 7b, respectively). The two planes have been selected at these coordinates to underline the differences on the flow below and above 50% span, as discussed for plane C in Figs. 3 and 4. The contour plots depict entropy distributions, by means of which it is possible to identify the vane and rotor wakes' convection in transonic stages (see for example Miller et al. [7]).

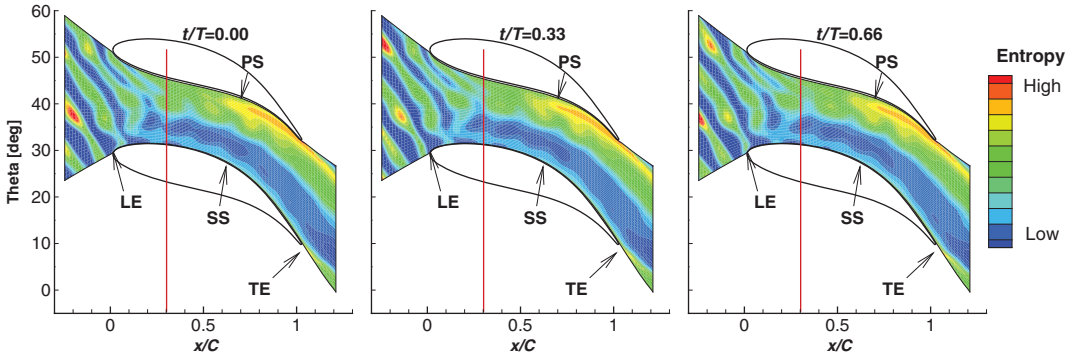


a) Plane at 50% span

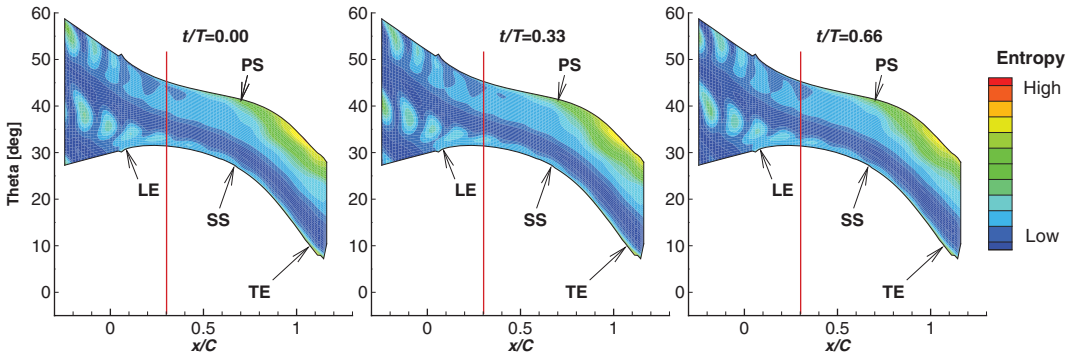


b) Plane at 30% span

**Fig. 7 Unsteady CFD: time-resolved entropy distribution in blade-to-blade planes at different channel heights. Rotor moves from bottom to top.**

The propagation of the HP rotor structures is clearly visible in Fig. 7a. These rotor structures can be identified as inclined lines at high entropy for $x/C < 0.3$. They move from the bottom to the top of the plot and their temporal evolution can be followed from $t/T = 0.00$ to $t/T = 0.66$. Local maxima of entropy within the rotor wakes appear at different positions for the different time snapshots. This is an effect of two different interactions: 1) the superposition of propagating stator wakes with the rotor wakes and 2) local increase of entropy due to rotor shocks "cutting" through the rotor wake.

As the wakes enter in the strut passage, they interact with the suction and pressure sides with different intensity. In the analyzed clocking position, the highest entropy is generated within the strut passage on the pressure side, as a result of the convection of high-entropy nuclei toward it. For $x/C > 0.3$, the unsteady disturbances induced by the upstream stage tends to decay. Therefore, the large unsteady pressure perturbations at $x/C > 0.3$, which are observed in Fig. 6, do not depend on the direct impingement of the HP rotor structures.

At 30% span (Fig. 7b), the distribution of the time-resolved entropy changes considerably. In fact, the rotor wakes cannot be observed in this plane. The contours at high entropy identify the HP vanes chopped segments (wake avenues) being convected within the TMTF passage. The structures move from the left to the right of the picture from $t/T = 0.0$ to $t/T = 0.66$. The comparison between Figs. 7b and 7a confirms the difference on the flow structure propagation observed in plane C (Figs. 3 and 4). Below 50% span, the most representative unsteady flow features are induced by the chopped structures of the HP vane; whereas, above 50% span, the unsteady flow features depend mostly on the impinging rotor structures. This is because of the large radial pressure gradient induced on the flow by the first bend of the diffusing duct.

The configuration of this two-stage facility plays a major role in the transport of unsteadiness through the TMTF. In fact, in counter-rotating turbines, because the upstream flow is preswirled, the turning required by the strut is reduced and therefore also the internal velocity gradients are lower than in a corotating turbine configuration. Typical effects of bowing and stretching of the unsteady incoming wakes [34] are reduced in this configuration. The chopped upstream vane segments (Fig. 7b) are mixed out after $x/C = 0.3$ because they directly impinge on the strut suction side. Similarly, the bowing of the rotor wakes occurs as soon as they enter in the strut passage (see Fig. 7a in the range $0 < x/C < 0.3$). According to the analytical model proposed in Chaluvadi et al. [35,36], the increasing in the vortex secondary kinetic energy through a blade row varies with the vortex-stretching ratio, which is only a function of the blade turning. Therefore, in a counter-rotating configuration, where the strut turning is reduced, the mixing losses associated with the convected vortices are expected to be lower.

Further information on the propagation of the unsteady structures is depicted in the meridional view of Fig. 8. The plot shows a time snapshot of the streamwise vorticity in the middle of the strut passage. The vorticities generated by the upstream stage are seen traveling through the entire TMTF passage and they can still be seen at the LP rotor inlet flow. Negative values show the tip leakage vortex and lower passage vortex, as identified from Fig. 4. The plane cuts the rotor structures, which can be observed as regions of negative or positive vorticity that are followed by regions of zero vorticity. Downstream of the strut leading edge at $x/C > 0.3$, the unsteadiness of the

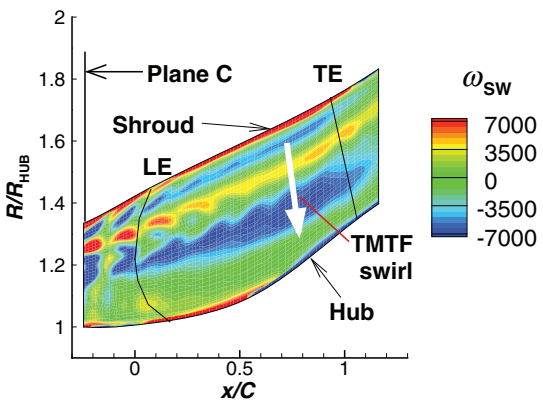


**Fig. 8 Unsteady CFD: time snapshot of time-resolved vorticity distribution in a meridional plane at 50% strut pitch.**

rotor tends to decay. However, the time-averaged vorticity does not decay; this is another effect of the counter-rotating setup that tends to enhance the time-averaged inlet vorticity, as largely described in Spataro et al. [27]. Further downstream, for $x/C > 0.5$, the swirl induced by the turning struts generates a strong radial gradient (see white arrow in Fig. 8) so that the low-energy cores are pushed toward the lower half-channel, and the same effect is induced by the second duct bend. This phenomena affects also the distribution of unsteady pressure fluctuations on the outlet plane, which will be addressed in the companion paper [22].

### C. Discussion

This section reports schematic representations (Fig. 9) of the interaction mechanisms that take place in a TMTF. Namely, the unsteady perturbations observed in the previous sections can be divided into 1) convection and decay of the HP rotor wakes and secondary flow structures (Fig. 9a); 2) convection and decay of HP vane structures that are chopped by the rotor (Fig. 9b); 3) effects of the TMTF potential field on the convection of the inlet unsteady disturbances (Fig. 9c); and 4) unsteady pressure fluctuations induced by the impingement of shock waves or reflected pressure waves (Fig. 9d).

The unsteady flow perturbations induced by the HP rotor, which are described in Fig. 4, can be divided in two main effects: velocity and angle nonuniformity induced by the blade wakes and secondary flows (as observed from the vorticity plot of Fig. 4a) and unsteady pressure perturbations (Fig. 4b) induced by the shock system. The periodic pressure fluctuations measured on the strut surface (Fig. 6) clearly depend on these two sources of deterministic unsteady stresses. However, as shown in Fig. 7a and schematically summarized in Fig. 9a, the blade-related flow structures, such as entropy defects due to the wake or secondary flows, mix out as soon as they are stretched and bowed by the strut potential field. After $x/C > 0.3$, the unsteady perturbation due to these effects starts to be negligible.

The flow structures related to the HP vane propagate through the HP rotor. They leave the HP vane following the absolute flow direction, then they are "turned" and "chopped" by the rotor blades, and they leave the rotor forming a series of segments on a well-defined direction referred to as the "wake avenue"(e.g., [7,34]). In the case of a low-aspect-ratio turbine, this wake avenue is formed mostly by secondary vortical flows, which play a more important role in the loss generation. However, the classical name is maintained here for clarity. Its effect on the downstream strut is clearly visible in Fig. 7b, as well as in the sketch of Fig. 9b, where the largest unsteady perturbation that directly impinges on the strut surface is due to these chopped segments of high entropy that propagate along a wake avenue.

The convection and propagation of the vane and blade structures is altered by the potential flowfield of the duct and of the strut. For example, the radial pressure gradients, such as that induced by the first duct bend, lead to large changes in the flow, as discussed comparing Figs. 7a and 7b at different spanwise heights. Similarly, the mutual interaction between the pressure field of the strut and of the HP vane (clocking) highly influences the unsteady pressure field on the strut itself, as analyzed in Fig. 6. These results highlight the effect of the HP vane chopped wake segments on the modulation of the HP rotor flowfield, as observed just downstream of the HP stage in Fig. 4 and at the inlet of the strut (e.g., Fig. 7a). Moreover, it confirms what is observed in Fig. 7b, that the upstream vane structures play a major role in the flow convection mechanism. Clocking, in the simplified view of Fig. 9b, can be represented as a circumferential shift of the wake avenues mutually influenced by the strut presence. The wake avenue of two clocking positions, namely, clock positions 24 and 9, are drawn in the plot. The potential field makes the wake avenue 24 impinge close to the leading edge, and the chopped vane segments are distorted by the potential pressure field. The wake avenue 9, representing the condition of the adjacent strut, travels through the middle of the passage, faces different pressure gradients, and impinges on a different location of the strut suction side.

Therefore, the clocking position governs the flow patterns that determine the level of stage mixing losses and overall unsteadiness.

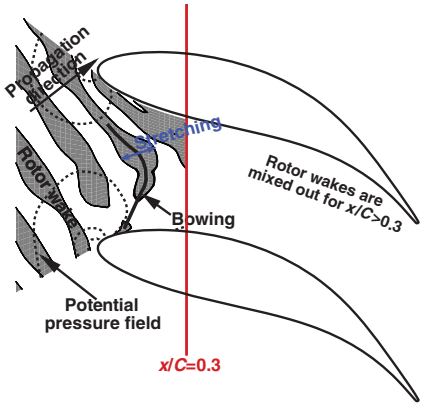


a) Schematic representation of the propagation of rotor-related structures

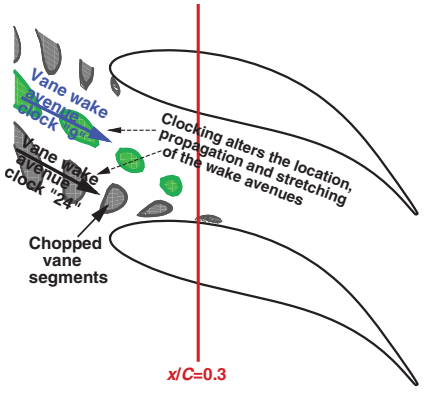


b) Schematic representation of the propagation of HP vane-related structures

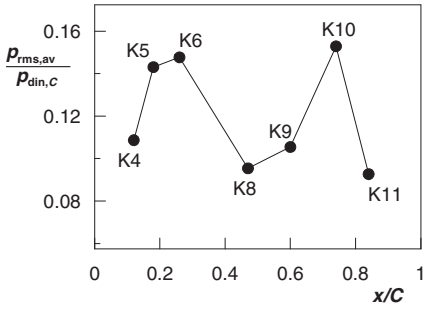


c) Average amplitude of rms of the deterministic fluctuations of pressure at different sensor positions

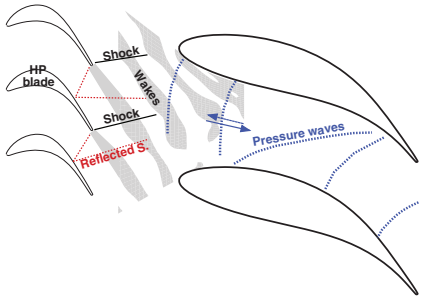


d) Schematic representation of the shock system downstream of the HP rotor and pressure wave propagation

**Fig. 9 Unsteady flow analysis: summary of main findings.**

In these kinds of stages, as observed in a one and a half transonic stage by Schennach et al. [37], three-dimensional clocking effects have to be expected (i.e., vortex interaction) playing a more dominant role in the stage efficiency than two-dimensional effects (i.e., wakes). (Even if these are generally 3-D structures, they can be reduced to two-dimensional structures for clocking studies that look at blade-to-blade planes.) These considerations are confirmed in the investigated setup: The pressure fluctuations at the strut inlet occur at the periodicity of the rotor structures and their intensity depends on the clocking position and span height at which they are investigated.

To observe the local effects of the strut loading distribution on the unsteady pressure fluctuations, the results from the 30 clocking positions have been further postprocessed. Figure 9c shows, for each sensor, an average value of the root mean square of the deterministic fluctuations of the pressure ($< p >_{\mathrm{rms,av}}$). The average is performed over the 30 clocking positions with the intent of removing the effect induced by the clocking itself. The result of this operation is made nondimensional by the average dynamic pressure in plane C and it is depicted in the ordinate of Fig. 9c for the different sensors. The plot summarizes two different effects and it should be read considering different series of sensors: K4–K6 located before $x/C = 0.3$ and K8–K11 located downstream of $x/C = 0.3$.

Sensor K6 presents the first maximum in the plot. This sensor is located at around $x/C = 0.3$. Upstream of this position, the unsteady flow features of the HP vane and blade are still dominating the flow in the passage of the strut and directly impinging on the strut suction side. Although the sensor K6 shows the largest average amplitude, it also presents the largest variation of amplitude due to the variation of clocking (see Fig. 6 and part 2 [22] for more details). This dependence on clocking can indicate that the overall large amplitude of the term $< p >_{\mathrm{rms,av}}$ is due to a direct impingement of the different unsteady flow features near the position of the sensor.

The second maximum in the distribution of Fig. 9c is for sensor K10. This is located far downstream of $x/C = 0.3$, in the strut throat, where the flow structures introduced by the HP stage are largely mixed out. Therefore, the large amplitude of the term $< p >_{\mathrm{rms,av}}$ is due to local velocity gradients: the maximum velocity within the strut is measured at this position and the unsteady pressure fluctuations are typically enhanced by the acceleration of the flow (i.e., the local velocity gradients).

In fact, the unsteady pressure fluctuations induced by the HP stage do not decay or mix out as the other flow structures as pictorially represented in Fig. 9d. Shock waves and reflected shock waves from the HP blades cut through the rotor wakes, locally enhancing the entropy within the wake (as discussed from Fig. 7a). Such waves, as well as the vortices shed by the rotor, induce pressure fluctuations that do not decay within the duct, but propagate downstream and locally impinge on the strut surface. Furthermore, the unsteady interaction of the rotor with the neighboring stators leads to pressure fluctuations with different propagation direction and intensity for adjacent blade passages (as depicted in Fig. 9d and previously discussed from Figs. 4b and 6).

The identification of a well-defined wave front (as seen with the dotted blue lines of Fig. 9d) is just pictorial. In a simple annular duct configuration, wave packets are propagating at different speeds and wave lengths [38]. When the duct is characterized by the interaction between rotating and static components, these wave packets are limited and related to the number of rotor and stator blades [39]. This phenomenon is even more complex in an S-shaped duct with embedded turning struts, where the unsteady pressure fluctuations can propagate upstream and they are circumferentially modulated by the interaction of blade/vane rows with unequal count. Hence, the discussion of such phenomena cannot be analyzed in terms of time-resolved quantities. Whenever the proper quantity is defined (e.g., the shock function), its analysis can help to identify local impingement of the unsteady fluctuations (see, for example, the work of Billiard et al. [40] on a one and half stage rig), but it does not provide a generic tool for the identification of deterministic stresses. This will be the purpose of the companion paper [22], which provides a method based on 2-D Fourier analysis to analyze deterministic stresses. The unsteady perturbations are considered as a superposition of azimuthal spinning modes (the 2-D Fourier coefficients), which are of limited number and can be easily related to the different sources of unsteadiness.

## IV. Conclusions

This two part paper presents and discusses the outcome of a numerical and experimental investigation on the unsteady flowfield through a two-stage counter-rotating turbine representative of an advanced architecture for future engine midturbine sectors. This first part focuses on the identification of the main patterns, which compose the three-dimensional unsteady nature of the fluid flowing from a high-speed transonic turbine to a low-pressure rotor placed downstream of the duct at higher radius.

An analysis of the midturbine frame carried out using a time-averaged approach (such as, for example, placing mixing planes between successive blade rows) seriously underestimates the overall component losses. Such an approach does not simulate the propagation of real features as wakes, vortices, and shocks convecting through the duct. Predicted data presented in this work have been validated by means of unsteady measurements performed upstream and within the duct. The agreement between CFD and experimental data suggests a good capability of commercial tools to capture the main contributors to the flow unsteadiness even with unsteady Reynolds-averaged Navier–Stokes calculations.

In the explanation of what was observed, the complexity of the flow was simplified, decoupling the influence of the principal design parameters. In particular, the role of key features acting either on the time-mean flow (i.e., S-shape duct meridional geometry, wide-chord/low-aspect-ratio turning struts, and turbines counter-rotating configuration) and on the time-resolved flow (e.g., rotor design as source of moving structures and clocking effects as influencer for interaction phenomena) was discussed.

The analysis of the unsteady pressure fluctuations within the TMTF passage shows that, whenever the vane–vane interaction effect is removed, the level of unsteadiness in the front part is governed by the convection of the upstream structures, whereas moving downstream in the passage, the perturbations are more sensitive to the local velocity and pressure gradient. The large fluctuations measured in the front part of the suction side are mainly due to the direct impingement of the rotor wakes and of the upstream chopped vane segments. The direct impingement is a characteristic feature of a counter-rotating configuration. A second maximum in such fluctuations corresponds to the turning struts' throat region where the higher local Mach number enhances the pressure perturbations. The results presented in this first part of the manuscript emphasize the error committed by neglecting the clocking effect on the effective local unsteadiness. A more general approach will be provided in the companion paper, where spectral analysis will take into account the turbine propagating modes.

Summarizing this study, there are three aspects of which a designer should be aware of to control the generation and propagation of aerodynamic deterministic stresses in midturbine sector stators: 1) the potential flowfield associated with the annulus line (duct aggressiveness) and to the vane shape (i.e., incidence distribution, velocity field distribution around the airfoil); 2) the design of the rotor and attention to its shed structures such as wakes, secondary vortices, and shocks; and 3) the choice of vane/blade count and clocking, as will be further discussed in the second part of the paper.

## Acknowledgments

The research leading to these results has been funded by the European Union (EU) within the EU project DREAM (contract ACP7-GA-2008-211861) as well as from the Austrian Ministry for Finance. The authors would like to thank H. Peter Pirker, Cornelia Santner, and Josef Hubinka for their important support during the experimental campaign.

## References


[1] Adamczyk, J. J., "Aerodynamic Analysis of Multistage Turbomachinery Flows in Support of Aerodynamic Design," *Journal of Turbomachinery*, Vol. 122, No. 2, 1999, pp. 189–217. doi:10.1115/1.555439

[2] He, L., "Fourier Methods for Turbomachinery Applications," *Progress in Aerospace Sciences*, Vol. 46, No. 8, 2010, pp. 329–341. doi:10.1016/j.paerosci.2010.04.001

[3] Tucker, P. G., "Computation of Unsteady Turbomachinery Flows: Part 1 Progress and Challenges," *Progress in Aerospace Sciences*, Vol. 47, No. 7, 2011, pp. 522–545. doi:10.1016/j.paerosci.2011.06.004

[4] Denton, J. D., and Singh, U. K., "Time Marching Methods for Turbomachinery Flows," *von Kármán Inst. Lecture Series*, Paper 1979-07, 1979.

[5] Adamczyk, J. J., "Model Equation for Simulating Flows in Multistage Turbomachines," American Soc. of Mechanical Engineers Paper 85-GT-226, Fairfield, NJ, 1985.

[6] Hodson, H. P., Hynes, T. P., Greitzer, E. M., and Tan, C. S., "A Physical Interpretation of Stagnation Pressure and Enthalpy Changes in Unsteady Flow," *Journal of Turbomachinery*, Vol. 134, No. 6, Nov. 2012, Paper 060902. doi:10.1115/1.4007208

[7] Miller, R. J., Moss, R. W., Ainsworth, R. W., and Horwood, C. K., "Time-Resolved Vane-Rotor Interaction in a High-Pressure Turbine Stage," *Journal of Turbomachinery*, Vol. 125, No. 1, Jan. 2003, pp. 1–13. doi:10.1115/1.1492823

[8] Norris, G., Dominy, R. G., and Smith, A. D., "Strut Influences Within a Diffusing Annular S-Shaped Duct," *Proceedings of ASME Turbo Exposition 1998*, American Soc. of Mechanical Engineers Paper 98-GT-425, Fairfield, NJ, 1998.

[9] Marn, A., Göttlich, E., Cadrecha, D., and Pirker, H. P., "Shorten the Intermediate Turbine Duct Length by Applying an Integrated Concept," *Journal of Turbomachinery*, Vol. 131, No. 4, July 2009, Paper 041014. doi:10.1115/1.3070578

[10] Göttlich, E., "Research on the Aerodynamics of Intermediate Turbine Diffusers," *Progress in Aerospace Sciences*, Vol. 47, No. 4, 2011, pp. 249–279. doi:10.1016/j.paerosci.2011.01.002

[11] Dènos, R., and Paniagua, G., "Rotor/Stator Interaction in Transonic HP Turbines," von Kármán Inst. Lecture Series Paper 2005-03, 2005.

[12] Miller, R. J., Moss, R. W., Ainsworth, R. W., and Harvey, N. W., "The Effect of an Upstream Turbine on a Low-Aspect Ratio Vane," *Proceedings of ASME Turbo Exposition 2004*, American Soc. of Mechanical Engineers Paper GT-2004-54017, Fairfield, NJ, 2004.

[13] Miller, R. J., Moss, R. W., Ainsworth, R. W., and Harvey, N. W., "The Development of Turbine Exit Flow in a Swan-Necked Inter-Stage Diffuser," *Proceedings of ASME Turbo Exposition 2003*, American Soc. of Mechanical Engineers Paper GT-2003-38174, Fairfield, NJ, 2003.

[14] Davis, R. L., Yao, J., Clark, J. P., Stetson, G., Alonso, J. J., Jameson, A., Haldeman, C. W., and Dunn, M. G., "Unsteady Interaction Between a Transonic Turbine Stage and Downstream Components," *International Journal of Rotating Machinery*, Vol. 10, No. 6, 2004, pp. 495–506. doi:10.1155/S1023621X04000491

[15] Haldeman, C. W., Krumanaker, M. L., and Dunn, M. G., "Influence of Clocking and Vane/Blade Spacing on the Unsteady Surface Pressure Loading for a Modern Stage and One-Half Transonic Turbine," *Journal of Turbomachinery*, Vol. 125, No. 4, Dec. 2003, pp. 743–753. doi:10.1115/1.1625398

[16] Göttlich, E., Marn, A., Pecnik, R., Malzacher, F. J., Schennach, O., and Pirker, H. P., "The Influence of Blade Tip Gap Variation on the Flow Through an Aggressive S-Shaped Intermediate Turbine Duct Downstream a Transonic Turbine Stage Part II: Time-Resolved Results and Surface Flow," *Proceedings of ASME Turbo Exposition 2007*, American Soc. of Mechanical Engineers Paper GT2007-28069, Fairfield, NJ, 2007.

[17] Lavagnoli, S., Yasa, T., Paniagua, G., Castillon, L., and Duni, S., "Aerodynamic Analysis of an Innovative Low Pressure Vane Placed in an S-Shape Duct," *Journal of Turbomachinery*, Vol. 134, No. 1, 2012, Paper 011013. doi:10.1115/1.4003241

[18] Lengani, D., Santner, C., Spataro, R., Paradiso, B., and Göttlich, E., "Experimental Investigation of the Unsteady Flow Field Downstream of a Counter-Rotating Two-Spool Turbine Rig," *Proceedings of ASME Turbo Exposition 2012*, American Soc. of Mechanical Engineers Paper GT2012-68583, Fairfield, NJ, 2012.

[19] Lengani, D., Santner, C., Spataro, R., and Göttlich, E., "Analysis Tools for the Unsteady Interactions in a Counter-Rotating Two-Spool Turbine Rig," *Experimental Thermal and Fluid Science*, Vol. 42, Oct. 2012, pp. 248–257. doi:10.1016/j.expthermflusci.2012.05.010

[20] Spataro, R., Göttlich, E., Lengani, D., Faustmann, C., and Heitmeir, F., "Development of a Turning Mid Turbine Frame with Embedded Design-Part I: Design and Steady Measurements," *Journal of Turbomachinery*, Vol. 136, No. 7, 2014, Paper 071008. doi:10.1115/1.4025949

[21] Spataro, R., Göttlich, E., Lengani, D., Faustmann, C., and Heitmeir, F., "Development of a Turning Mid Turbine Frame with Embedded Design-Part II: Unsteady Measurements," *Journal of Turbomachinery*, Vol. 136, No. 7, 2014, Paper 071012. doi:10.1115/1.4025950

[22] Lengani, D., Spataro, R., Peterleithner, J., and Göttlich, E., "Unsteady Flow Features Evolution Through a Turning Midturbine Frame Part 2: Spectral Analysis," *Journal of Propulsion and Power* (to be published).

[23] Hubinka, J., Santner, C., Paradiso, B., Malzacher, F., Göttlich, E., and Heitmeir, F., "Design and Construction of a Two Shaft Test Turbine for Investigation of Mid Turbine Frame Flows," *19th International Symposium on Airbreathing Engines*, AIAA Paper ISABE-2009-1293, 2009.

[24] Hubinka, J., Paradiso, B., Santner, C., Göttlich, E., and Heitmeir, F., "Design and Operation of a Two Spool High Pressure Test Turbine Facility," *Proceedings of the Ninth European Turbomachinery Conference*, 2011, Paper 112.

[25] Persico, G., Gaetani, P., and Guardone, A., "Design and Analysis of New Concept Fast-Response Pressure Probes," *Measurement Science and Technology*, Vol. 16, No. 9, 2005, pp. 1741–1750. doi:10.1088/0957-0233/16/9/005

[26] Hussain, A., and Reynolds, W., "The Mechanics of an Organized Wave in Turbulent Shear Flow," *Journal of Fluid Mechanics*, Vol. 41, No. 2, 1970, pp. 241–258. doi:10.1017/S0022112070000605

[27] Spataro, R., Santner, C., Lengani, D., and Göttlich, E., "On the Flow Evolution Through a LP Turbine with Wide-Chord Vanes in an S-Shaped Channel," *Proceedings of ASME Turbo Exposition 2012*, American Soc. of Mechanical Engineers Paper GT2012-68178, Fairfield, NJ, 2012.

[28] *ANSYS CFX-Solver Modeling Guide*, ANSYS, Ver. 13.0, Canonsburg, PA, 2010.

[29] Menter, F. R., "Two-Equation Eddy-Viscosity Turbulence Models for Engineering Applications," *AIAA Journal*, Vol. 32, No. 8, 1994, pp. 1598–1605. doi:10.2514/3.12149

[30] Santner, C., Paradiso, B., Malzacher, F., Hoeger, M., Hubinka, J., and Göttlich, E., "Evolution of the Flow Through a Turning Mid Turbine Frame Applied Between a Transonic HP Turbine Stage and a Counter-Rotating LP Turbine," *Proceedings of the Ninth European Turbomachinery Conference*, 2011, Paper 110.

[31] Paradiso, B., Santner, C., Hubinka, J., Göttlich, E., and Hoeger, M., "Turning Mid Turbine Frame Behavior for Different HP Turbine Outflow Conditions," *Proceedings of ASME Turbo Exposition 2011*, American Soc. of Mechanical Engineers Paper GT2011-46506, Fairfield, NJ, 2011.

[32] Paradiso, B., Persico, G., Gaetani, P., Schennach, O., Pecnik, R., and Woisetschläger, J., "Blade Row Interaction in a One and a Half Stage Transonic Turbine Focusing on Three Dimensional Effects Part I: Stator-Rotor Interaction," *Proceedings of ASME Turbo Exposition 2008*, American Soc. of Mechanical Engineers Paper GT2008-50291, Fairfield, NJ, 2008.

[33] Göttlich, E., Woisetschläger, J., Pieringer, P., Hampel, B., and Heitmeir, F., "Investigation of Vortex Shedding and Wake-Wake Interaction in a Transonic Turbine Stage Using Laser-Doppler-Velocimetry and Particle-Image-Velocimetry," *Journal of Turbomachinery*, Vol. 128, No. 1, 2006, pp. 178–187. doi:10.1115/1.2103092

[34] Hodson, H. P., and Howell, R. J., "The Role of Transition in High Lift Low Pressure Turbines for Aero Engines," *Progress in Aerospace Science*, Vol. 41, No. 6, Aug. 2005, pp. 419–454. doi:10.1016/j.paerosci.2005.08.001

[35] Chaluvadi, V. S. P., Kalfas, A. I., Hodson, H. P., Ohyama, H., and Watanabe, E., "Blade Row Interaction in a High-Pressure Steam Turbine," *Journal of Turbomachinery*, Vol. 125, No. 1, 2003, pp. 14–24. doi:10.1115/1.1518504

[36] Chaluvadi, V. S. P., Kalfas, A. I., Banieghbal, M. R., Hodson, H. P., and Denton, J. D., "An Experimental Study of the Unsteady Characteristics of the Turbulent Wake of a Turbine Blade," *Journal of Propulsion and Power*, Vol. 17, No. 4, 2001, pp. 892–901. doi:10.2514/2.5821

[37] Schennach, O., Woisetschläger, J., Paradiso, B., Persico, G., and Gaetani, P., "Three Dimensional Clocking Effects in a One and a Half

Stage Transonic Turbine," *Journal of Turbomachinery*, Vol. 132, No. 1, 2010, Paper 011019.
doi:10.1115/1.3072715

[38] Rienstra, S. W., and Hirschberg, A., *Introduction to Acoustics*, Eindhoven Univ. of Technology, Eindhoven, The Netherlands, 2004, pp. 199–235.

[39] Tyler, J. M., and Sofrin, T. G., "Axial Flow Compressor Noise Studies," *SAE Transactions*, Vol. 70, 1962, pp. 309–332.

[40] Billiard, N., Jerez Fidalgo, V., Dènos, R., and Paniagua, G., "Analysis of Stator-Stator Clocking in a Transonic Turbine," *Proceedings of ASME Turbo Exposition 2007*, American Soc. of Mechanical Engineers Paper GT2007-27323, Fairfield, NJ, 2007.